PAPER

Electrical transport properties in Ge hyperdoped with Te

View the article online for updates and enhancements.

Electrical transport properties in Ge hyperdoped with Te

D Caudevilla[1,*] , **S Algaidy**[1] , **F Pérez-Zenteno**[1] , **S Duarte-Cano**[1] ,
R García-Hernansanz[1,*] , **J Olea**[1] , **E San Andrés**[1] , **A del Prado**[1] , **R Barrio**[2] ,
I Torres[2] , **E García-Hemme**[1] and **D Pastor**[1,*]

[1] Dpto. Estructura de la Materia, Física Térmica y Electrónica, Universidad Complutense de Madrid, Fac.
de CC. Físicas. Plaza de Ciencias 1, E-28040 Madrid, Spain
[2] Unidad de Energía Solar Fotovoltaica, Dpto. de Energías Renovables, CIEMAT. Av. Complutense 40,
E-28040 Madrid, Spain

E-mail: danicaud@ucm.es, eric.garcia@ucm.es and dpastor@ucm.es

CrossMark

Abstract

In this work we have successfully hyperdoped germanium with tellurium with a concentration
peak of 10^{21} cm^{-3}. The resulting hyperdoped layers show good crystallinity and sub-bandgap
absorption at room temperature which makes the material a good candidate for a new
era of complementary metal-oxide-semiconductor-compatible short-wavelength-infrared
photodetectors. We obtained absorption coefficients α higher than 4.1×10^3 cm^{-1} at least up to
3 μm. In this study we report the temperature-dependency electrical properties of the
hyperdoped layer measured in van der Pauw configuration. The electrical behaviour of this
hyperdoped material can be explained with an electrical bilayer coupling/decoupling model and
the values for the isolated hyperdoped layer are a resistivity of 4.25×10^{-3} Ω·cm with an
electron-mobility around -100 cm^2 V^{-1} s^{-1}.

(Some figures may appear in colour only in the online journal)

1. Introduction

In the last years, short-wavelength-infrared (SWIR; 1–3 μm)
detection has been attracting a great interest because its
many applications, including biomedical imaging, surveil-
lance, chemical sensing and long-haul-communications [1–3].
This market is dominated by group III-V and II-VI compounds
such as InGaAs, InP, Hg$_{1-x}$Cd$_x$Te [4, 5]. However, these
semiconductors are scarce, toxic and are not easily integrated
with the read-out complementary metal-oxide-semiconductor
(CMOS) circuitry, which increases the size and cost of a final
device. Moreover, most of these devices require cooling at
liquid nitrogen temperature, increasing the dimensions and
price of the device [6].

However, Si and Ge semiconductors are easily integrated
with the standard CMOS technology. It has been demonstrated
that the semiconductor can be hyperdoped introducing con-
centrations of deep-level donors such as Ti, Te, Se or Au with
concentrations above the solid solubility limit. Some of these
semiconductors exhibit sub-bandgap room-temperature pho-
todetection. The reason for this response can be explained by
the formation of an impurity band (IB). This band would allow
the absorption of photons with energies not only above the
bandgap energy, but also with lower energies. This absorption
process promotes carriers from the valence band to the IB and
from the IB to the conduction band [7–13]. Also, the signal-
to-noise ratio of these hyperdoped devices is better than the
conventional detectors and can be used at room temperature.
Thus, these detectors could be easily incorporated into low-
cost appliances, namely smart-phones. Several other materials
based on hyperdoping and the IB concept have been studied

* Authors to whom any correspondence should be addressed.

since the 1960s and new materials are still being developed today for sub-bandgap sensing, such as black diamond and hyperdoped-diamond [14, 15].

In this field, Si has been extensively studied, but there is an important lack of information about the Ge hyperdoped properties. In this work we focus on Ge because it already responds up to 1870 nm and the carrier mobilities are higher than in Si. There are different techniques to obtain hyperdoped materials [16], but in this work we focus on the combination of two out-of-the-equilibrium techniques: ion implantation followed by pulsed laser melting (PLM) [10, 12]. With ion implantation we can introduce atoms at very high concentrations. In this case we have chosen tellurium because it is a deep-level donor in germanium, it already has high maximum solid solubility limit around 2×10^{15} [17] and low diffusion coefficient (10^{-11} cm^2 s^{-1} at 920 °C [17]), which will allow us to incorporate more impurities to the lattice. After implantation, an ultra-fast recrystallization, using PLM, is required to recover the crystallinity of the sample and activate the impurities while minimising the dopant diffusion.

The feasibility of the Ge hyperdoped with Te has already been proven [13]. In this work we study in detail the structural and optical properties of this material and focus on the electronic properties of the bilayer structure. We apply a bilayer model to the van der Pauw measurements and extract the electronic properties of the hyperdoped layer.

2. Experimental

2.1. Samples fabrication

A n-type germanium wafer (100) with a 300 μm thickness and 1–3 Ω·cm resistivity was implanted with ^{130}Te$^+$ in a IBS refurbished VARIAN CF3000 ion implanter. The implantation energy set was 74 keV and the dose was 10^{15} cm^{-2}. The sample was tilted 7° to reduce channelling and the holder was refrigerated with liquid nitrogen (LN$_2$) to avoid ion-implantation-related porosity [18–20]. This porosity effect has been attributed to the migration of the germanium vacancies forming clusters during the implantation process. It has been observed that this clustering process is very dependent on the temperature. We measured the temperature on the surface of the sample prior to the implantation and it was around 80 K.

After ion implantation, square-shaped samples were pulsed-laser melted (PLM) with a Nd:YAG laser working at its third harmonic wavelength (355 nm). The pulse duration was 4 ns and the energy 260 mJ, which corresponds to a fluence of 331 mJ·cm^{-2} in a circular spot of 10 mm diameter. During this pulse, the top surface of the sample is melted beyond the amorphized region and afterwards it recrystallizes taking the substrate as seed, via solid-phase epitaxy. The speed of this recrystallization is so fast that the Te-impurities are trapped into the semiconductor lattice.

2.2. Structural characterization

Scanning electron microscopy (SEM) images were taken with a JEOL JSM 7600F working at 15 kV acceleration voltage to inspect the surface of the implanted samples.

We performed time-of-flight secondary ion mass spectroscopy (ToF-SIMS) to analyse the Te profile in depth. The experiments were done in negative polarity, obtained by a ToF-SIMS 4, manufactured by ION-TOF. Bi^{3+} was used as the primary ion at 25 keV pulsed beam tilted 45° for analysis and a Cs gun energy of 1 keV as sputtering source.

To check the crystal quality of the samples we used Raman spectroscopy with an excitation wavelength of 532 nm, which is absorbed approximately during the first 20 nm of the sample, so it gives us information about the implanted layer. We used a high resolution diffraction grating Echelle 75/64 and an objective of 20x/0.45. We focus on the Raman shift range from 163 to 196 cm^{-1}, with a resolution of 0.22 cm^{-1}.

2.3. Optical characterization

For the optical characterization we measure the transmittance $T(\lambda)$ and specular reflectance $R(\lambda)$ in normal incidence with a UV/Visible/NIR PerkinElmer Lambda 1050 spectrophotometer in the range 400–3000 nm. We calculate the total absorptance of the sample as $A(\lambda) = 1 - T(\lambda) - R(\lambda)$.

We can calculate the absorption coefficient of the implanted layer at wavelengths longer than the bandgap (1870 nm) if we follow some simplifying assumptions [11]:

- The substrate absorption coefficient is negligible and the thickness of the substrate is much higher than the wavelength, so we can neglect the interference effect on the calculations.
- The refractive index of the implanted layer is very similar to the one of the virgin Ge, so there is no refraction between the implanted layer and the substrate.

Then, the system can be modelled as a layer surrounded by air where the incoming light transmitted into the layer is reflected multiple times and each time that it is reflected there is some absorption. The total absorbance is the sum and can be expressed as a geometric series:

$$A(\lambda) = \sum_{n=0}^{\infty} I_0 t a (1-a)^n r^n = \frac{I_0 t a}{1 - r(1-a)}, \qquad (1)$$

where I_0 is the incident intensity, $t \equiv t(\lambda)$ is the wavelength-dependent transmission coefficient between air and Si, $r \equiv r(\lambda)$ is the reflection coefficient for each wavelength between Si and air, and $a(\lambda)$ is the absorption term resulting from each time light travels through the implanted layer. This term is defined as $a(\lambda) = \exp(-\alpha d)$, where $\alpha \equiv \alpha(\lambda)$ is the absorption coefficient and d is the effective thickness of the absorbing layer. We can apply the same model to extract the absolute transmitted and reflected light after multiple reflections. These

expressions also follow a geometric series (see Supplementary Material section) and their sum is equal to the incident light.

2.4. Electrical characterization

Some samples were cut in square shape and 200 nm Ni contacts were deposited by e-beam evaporation on the corners, in van der Pauw configuration. The contacts were connected through 4 SMU probes to a Keithley SCS 4200 model and the samples were kept inside a Janis cryostat which allows us to measure from 300 K to 15 K. We measured the sheet conductance (G_S) in the four possible configurations feeding with 1 mA. The current was injected in both directions, thus we measured eight configurations in total. We also measured the Hall effect injecting the current in opposite contacts and applying a 0.9 T magnetic field. This magnetic field was also applied in both perpendicular directions to the sample, resulting in 16 configurations for the Hall effect. The electromagnet was powered with a bipolar Kepco BOP 50-20MG power supply.

To analyse the behaviour of the hyperdoped samples we apply the bilayer model proposed in [21], since the hyperdoped layer is electrically coupled to the substrate depending on the temperature. This model describes the electrical properties of a two-layers system:

$$G_S = \frac{\ln 2}{\pi} \frac{I}{\Delta V} = \frac{(G_{S1} + G_{S2}F)^2}{G_{S1} + G_{S2}F^2} \tag{2}$$

$$\mu = -\frac{G_S \Delta V_{HALL}}{IB} = \frac{\mu_1 G_{S1} + \mu_2 G_{S2}F^2}{G_{S1} + G_{S2}F^2}, \tag{3}$$

where G_S is the measured sheet conductance of the bilayer system, and it is the result of the combination of the sheet conductance of each layer ($G_{S1,2}$). In a similar way, the mobility (μ) of the system is given by the average mobilities weighted by the conductance of each layer ($\mu_{1,2}$). The contribution of the substrate (G_{S2} and μ_2) to the measurement depends on the coupling factor F, which varies from 0 to 1. In the regions where the F parameter is known we can extract the properties of the implanted layer.

3. Results and discussion

3.1. Structural results

Ion implantation at LN_2 temperature has been realised to avoid surface porosity [18]. In figure 1 we show the surface morphology obtained by SEM of the implanted samples at (a) LN_2 and (b) room temperature (RT). The sample implanted at room temperature is fully porous and the sample implanted at LN_2 temperature shows a similar surface than an unimplanted sample, corroborating that implanting at LN_2 temperatures avoids the formation of porous structures.

In figure 2 we show the measured Te concentration depth profile for an as-implanted sample and a sample after the laser melting obtained by ToF-SIMS. It is also represented the Monte-Carlo stopping and range of ions in matter (SRIM)

simulation of a 74 keV implantation at RT. We can observe that the Te profile of the as-implanted sample does not follow the SRIM simulation. When implanting at LN_2 temperatures, the profile is shifted closer to the surface. During the implantations we also implanted control samples with lithography structures and we did not observe significant differences in topography between the implanted and unimplanted regions, which rules out the possibility of a relevant sputtering during the implantation. The explanation for this difference between the measured profile shifted to the surface and the SRIM simulation is not clear but has also been observed when implanting different ions at low temperatures in other materials [22]. Even with this discrepancy between simulation and experiments, these results demonstrate that we have overcame the solid solubility limit of Te in Ge by more than five orders of magnitude in the first 23 nm.

After the PLM process, the Te impurities have been redistributed around the first 10 nm, where we have a maximum concentration of $1.1 \times 10^{21} \, cm^{-3}$. The impurity concentration to surpass the insulator to metal transition and form an IB is nominally $5.9 \times 10^{19} \, cm^{-3}$, but depends on the host semiconductor and the impurity [8]. We overcome the insulator to metal transition in the first 35 nm and the solid solubility limit in the fully implanted region. For the calculations during this work we will take 35 nm as the reference effective thickness of the hyperdoped layer.

In figure 3 we show the Raman spectra for the germanium reference sample, the as-implanted sample, and the PLM sample. During the implantation, the sample surfaces become amorphous and this is pointed out by the a-Si band around 250–300 cm^{-1} of the implanted spectrum. We do not observe any crystalline signal in the as-implanted samples, meaning that all the light is absorbed in the implanted region. However, after the PLM process, the crystallinity of the sample is fully recovered, as the crystalline Ge–Ge peak at 300 cm^{-1} indicates. This peak is almost identical in shape as the peak from a Ge reference sample. The observed downshift of less than 1 cm^{-1} would be related to lattice strain due to the Te incorporation in the Ge lattice.

3.2. Optical results

3.2.1. Transmittance. After producing a high crystallinity implanted layer with Te concentration well above its solid solubility limit, we measure the transmittance and reflectance to determine the optical activation of that impurities. First, we measure the transmittance of the samples (figure 4(a)). Light up to 1870 nm (band-gap of Ge: 0.66 eV) is either reflected in the substrate or absorbed in the substrate. For longer wavelengths, the substrate is not absorbing, so the transmittance difference between the reference sample and the implanted samples is because of multiple reflections or the absorption of the implanted layer.

3.2.2. Reflectance. In figure 4(b) we have represented the reflectance measurements. In the reference sample we can clearly observe that the reflectance comes from the reflectance
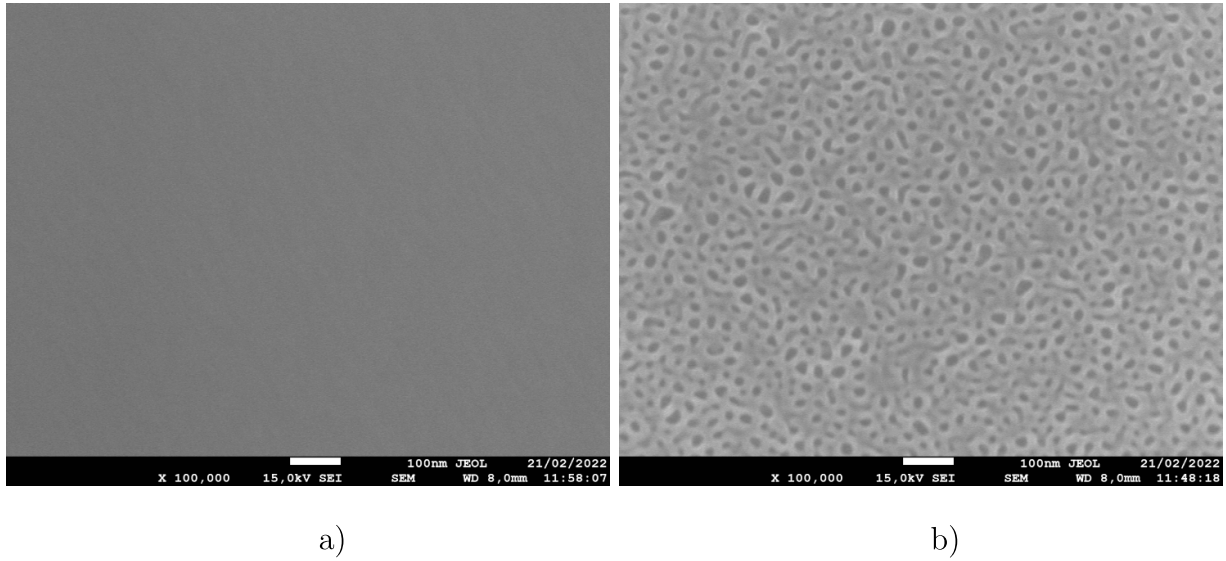
Figure 1. SEM images of the surface of Te-implanted Ge with a dose of $10^{15}\,\mathrm{cm}^{-2}$ at different temperatures: (a) liquid-nitrogen temperature and (b) room temperature.
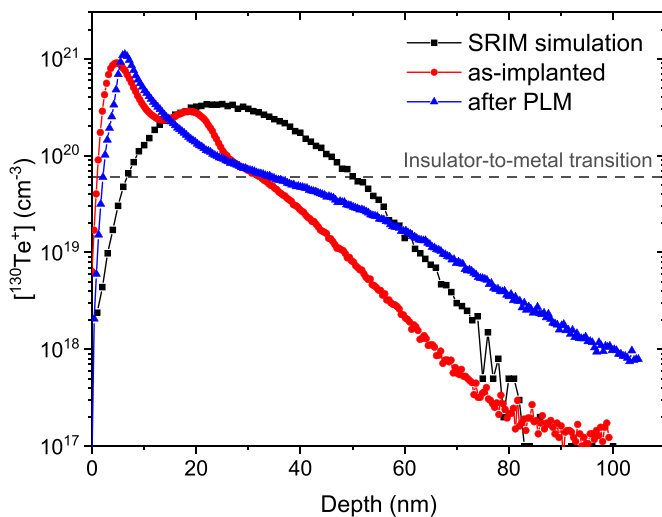

Figure 2. ToF-SIMS measurements of as- implanted and PLM samples together with the SRIM simulation at RT. It is also highlighted the insulator to metal transition [8].
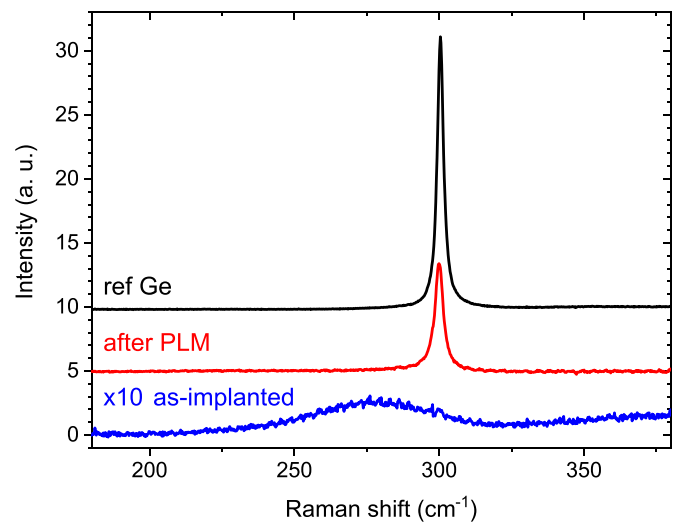

Figure 3. Raman spectra of a virgin Ge sample, a Te as-implanted amorphized sample and a Te-implanted sample recrystallized by PLM (for the sake of clarity, the spectra are shifted vertically).

of the top surface for wavelengths below 1870 nm; and above, the reflected light comes from the top surface reflectance but also from the back surface, since the germanium is transparent at those wavelengths. The as-implanted sample differs from the reference at sub-bandgap wavelengths due to the amorphization of the implanted layer. At wavelengths above Ge bandgap, the reflectance is slightly reduced most probably because the induced defects are absorbing part of the light [23]. However, the PLM sample recovers a shape of the curve very similar to the Ge substrate, which was expected because we recovered the crystallinity. However, after the PLM, the sample recovers the crystallinity, since it can be observed to have a similar behaviour than the Ge substrate. Furthermore, in the PLM sample, the reflectance is lower for wavelengths above the bandgap, and this can be explained

with the absorption of the hyperdoped layer. The reflectance of the PLM is also lower for wavelengths below 750 nm, most probably because the refractive index is changed at those wavelengths.

3.2.3. Absorptance. Subtracting the transmittance and the reflectance to the 100% we can obtain the light which is absorbed in our samples (figure 5). If we focus on the wavelengths longer than 1870 nm (which corresponds to 0.66 eV, the energy of the bandgap), we corroborate that the absorptance of the reference Ge sample is negligible. The physical reason behind this is that the energy of the photons is not enough to overcome the bandgap energy ($E < E_{gap}$) and they are not absorbed. For the as-implanted sample, around 2%
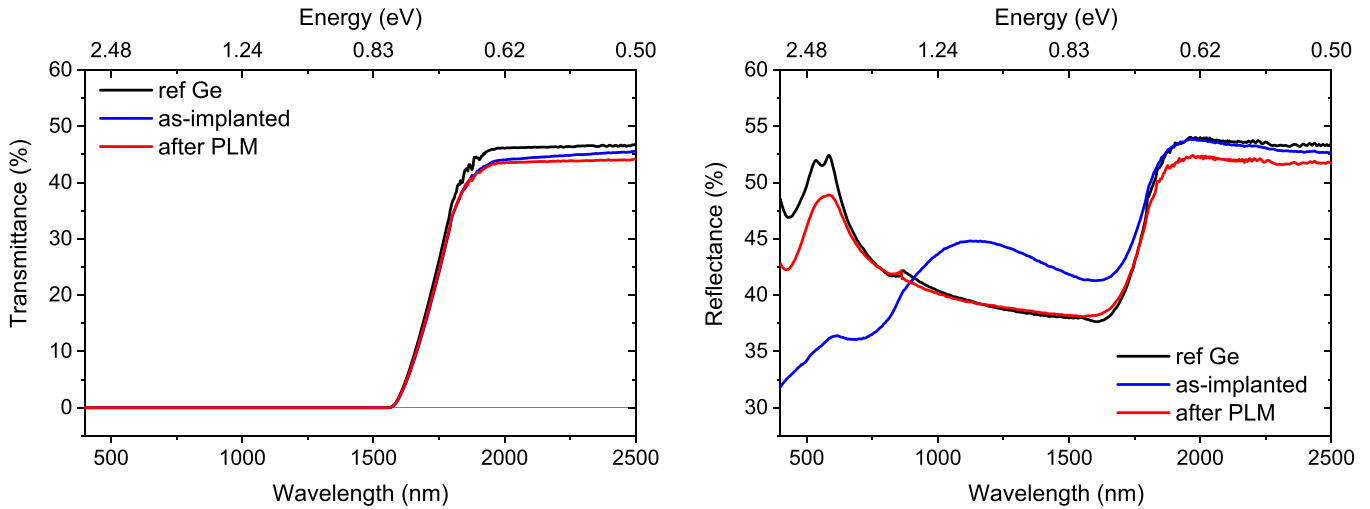
Figure 4. Optical measurements: transmittance (left) and reflectance (right) of a reference Ge sample, an as-implanted sample and a recrystallized PLM sample.
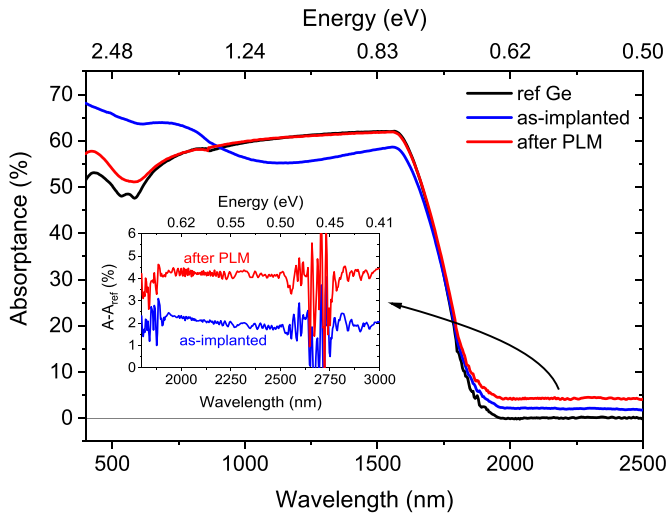

Figure 5. Absorptance of a reference Ge-sample, a Te-implanted sample and a recrystallized Ge:Te sample. In the inset it is plotted the absorption difference in % between the implanted samples with respect to the reference Ge sample for wavelengths between 2000 and 3000 nm.

of the light is absorbed in the implanted region, most probably because of defects and the amorphous character of the layer. The PLM-recrystallized sample has even higher absorptance than the as-implanted sample. Also, as it has been shown by Raman spectroscopy, it exhibits better crystal quality. Thus, we associate this sub-bandgap absorption to extrinsic defects introduced by the ion implantation followed by the PLM process. The total absorption of this sample is around 4%, and applying the equations given in section 2.3 it corresponds to a factor αd of 4.1×10^{-2}, which is in agreement with the values previously reported for similar doses [13]. If we consider that the layer depth where we overcome the insulator to metal transition (35 nm) is the thickness of the absorbing layer above 1870 nm we can set an upper limit for the

absorption coefficient of $1.2 \times 10^4 \, \text{cm}^{-1}$, and taking 100 nm as the thickness of the absorbing layer we set the lower limit to $4.1 \times 10^3 \, \text{cm}^{-1}$. The most probable scenario is that the implanted layer is changing the absorption coefficient according to the tellurium profile and the total absorptance comes from integrating the whole profile. In any case those limits show that the absorption coefficient is more than 5 orders of magnitude higher than for virgin Ge, in agreement with previous results [13]. These values are in the same order of magnitude as the highest absorption coefficients obtained from hyperdoped silicon [11, 24].

3.3. Electrical results

The electrical properties of the hyperdoped layer on n-type substrates present a temperature-dependence decoupling effect, as shown in figure 6. In this graph, it can be observed that the sheet conductance (G_S) tendency of the implanted sample is similar to the sheet conductance of a measured substrate (G_{S2}) for temperatures ranging from 300 K down to 200 K, so in this region we conclude that both layers are totally coupled ($F = 1$). As the temperature decreases, the hyperdoped layer starts to be electrically decoupled from the substrate ($F < 1$), unveiling the properties of the hyperdoped layer as if it would be isolated. In figure 7, the differences between the reference Ge sample and the hyperdoped sample can be observed. As expected, the mobility of the reference sample increases as the temperature decreases as a result of a lower interaction with the phonons of the lattice. In contrast, for the hyperdoped sample, the mobility decreases as the temperature decreases, which falls down reaching values around $-100 \, \text{cm}^2 \, \text{V}^{-1} \, \text{s}^{-1}$ for temperatures in the 20–100 K region. The measured mobility is electron-dominated for the whole range of temperatures (20–300 K). These results are in good agreement with previously reported results of similar hyperdoped structures, such as Si:Ti [21] and Si with other transition metals (Cr, V) [25].
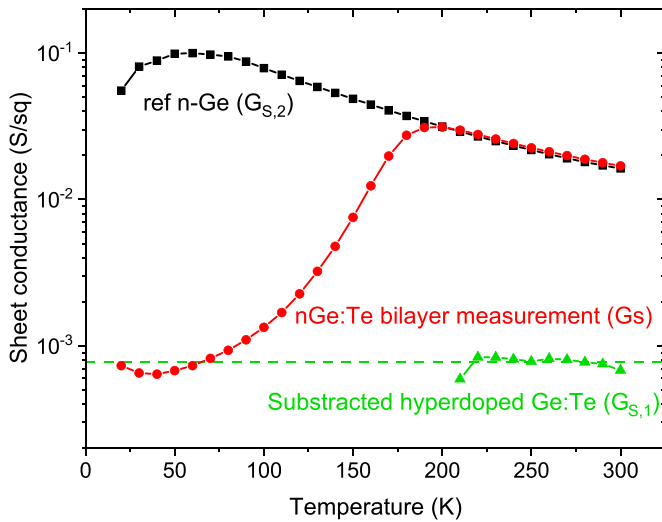
Figure 6. Sheet conductance (G_S) of a reference n-Ge substrate (■) and a Te-implanted sample and recrystallized by PLM (●). It is also represented the sheet resistance extracted values of the hyperdoped layer with a guide to the ere with the mean value in the region from 200 to 300 K.
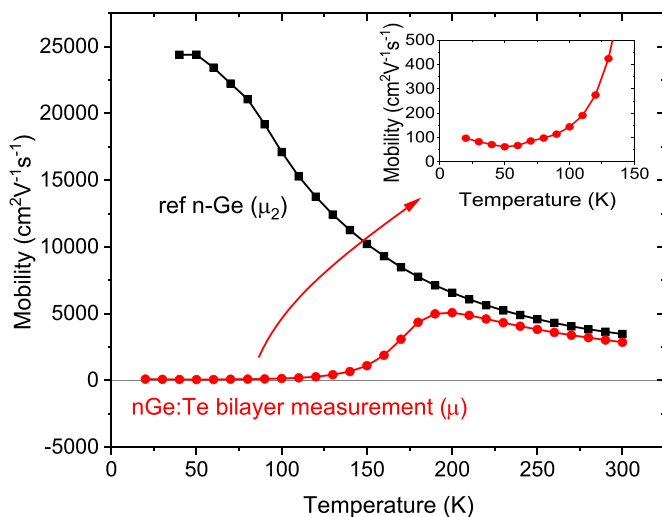

Figure 7. Measured hall mobility as a function of the temperature in van der Pauw configuration of a reference sample and an implanted and PLM sample. The inset is a zoom in the 0–150 K temperatures region for the values of the hyperdoped sample.

If we apply the model described in 2.4 with $F = 1$ in the region where the layers are totally coupled, we can extract the values of the sheet conductance of the hyperdoped layer, which is shown in figure 6, just by subtracting the sheet conductance of the substrate to the measured value. We can observe that these values are constant among that region, as it is expected from a hyperdoped metallic layer, and it is also plotted a dashed line of the mean value as a guide to the eye, since this value is in the same order of the sheet conductance values of the bilayer system when the implanted layer is isolated from the substrate. These values correspond to 235 S·cm^{-1} if we consider that the thickness of the layer

is the depth where we overcome the insulator to metal transition. For mobility and sheet concentration measurements we cannot apply the model because the differences between the sheet conductance multiplied by the mobility of both measurements are very similar; then the error is high: for example, a difference of just a 5% in the mobility or concentration of the substrate parameters means a variation on the layer mobility values from $-10\,000$ to $1800\,\text{cm}^2\,\text{V}^{-1}\,\text{s}^{-1}$, which is not consistent and makes no physical sense. To better analyse the electrical properties of this system it is convenient to implant higher doses, and then the implanted layer will increase the contribution to the measured values.

The measured values at low temperature correspond to electrical measurements of the isolated hyperdoped layer. This layer presents a conductivity of $235\,\text{S·cm}^{-1}$, a mobility of $-100\,\text{cm}^2\,\text{V}^{-1}\,\text{s}^{-1}$ and an effective electron carrier concentration of around $1.5 \times 10^{19}\,\text{cm}^{-3}$. This carrier concentration is slightly lower than the theoretical insulator to metal transition concentration for the IB formation. Since we observe at low temperature the metallic behaviour associated to the IB formation, this threshold could be lower for this specific system formed by the Ge and the Te, or the effective thickness considered for the hyperdoped semiconductor is slightly lower. In any case the carrier concentration value is several orders above the solid solubility limit and in the order of the theoretical insulator to metal transition limit.

4. Conclusion

In this work we have successfully implanted Ge with Te with a peak concentration of $10^{21}\,\text{cm}^{-3}$ recovering the crystallinity of the samples after a laser annealing process. We obtain a crystalline hyperdoped layer which overcomes the insulator to metal transition the first 35 nm showing sub-bandgap absorption at room temperature and an absorption coefficient around $1.2 \times 10^4\,\text{cm}^{-1}$ in agreement with previous reports. We analysed the electrical properties of the implanted samples and observe a temperature-dependency coupling effect very similar to other hyperdoped materials which are also suitable for infrared sensing.

Using an electrical bilayer model, we can explain the electrical measured behaviour assuming an electrical decoupling of the hyperdoped and Ge substrate layers. Since the hyperdoped layer is electrically isolated at low temperatures we can measure the electrical transport measurements of the hyperdoped semiconductor.

Data availability statement

The data that support the findings of this study are available upon reasonable request from the authors.

Acknowledgments

Supplementary material

Equations used for transmittance and reflectance considering multiple reflections between the hyperdoped layer and air:

$$R = I_0 r + I_0 t^2 r (1-a)^2 + I_0 t^2 r^3 (1-a)^4 + I_0 t^2 r^5 (1-a)^6 + \cdots$$

$$= I_0 r + I_0 r t^2 (1-a)^2 \sum_{n=0}^{\infty} [r(1-a)]^{2n}$$

$$= I_0 r \left[1 + \frac{t^2(1-a)^2}{1 - r^2(1-a)^2} \right] \tag{4}$$

$$T = I_0 t^2 (1-a) + I_0 t^2 r^2 (1-a)^3 + I_0 t^4 r^2 (1-a)^5 + \cdots \tag{5}$$

$$= I_0 t^2 (1-a) \sum_{n=0}^{\infty} [r(1-a)]^{2n} = \frac{I_0 t^2 (1-a)}{1 - r^2 (1-a)^2}.$$

ORCID iDs

D Caudevilla ● https://orcid.org/0000-0002-8479-2644
S Algaidy ● https://orcid.org/0000-0002-1164-6267
F Pérez-Zenteno ● https://orcid.org/0000-0002-6509-6010
S Duarte-Cano ● https://orcid.org/0000-0003-4184-0332
R García-Hernansanz ● https://orcid.org/0000-0002-8419-8012
J Olea ● https://orcid.org/0000-0002-7200-0371
E San Andrés ● https://orcid.org/0000-0003-3432-9915
A del Prado ● https://orcid.org/0000-0003-0633-9462
R Barrio ● https://orcid.org/0000-0001-7662-0714
I Torres ● https://orcid.org/0000-0002-9971-3988
E García-Hemme ● https://orcid.org/0000-0001-5328-8341
D Pastor ● https://orcid.org/0000-0003-2975-3973

References

[1] Hansen M P and Malchow D S 2008 Overview of SWIR detectors, cameras and applications *Proc. SPIE* **6939** 94–104

[2] Soref R 2015 Enabling 2 μm communications *Nat. Photon.* **9** 358–9

[3] Berencén Y *et al* 2018 CMOS-compatible controlled hyperdoping of silicon nanowires *Adv. Mater. Interfaces* **5** 1800101

[4] Manda S *et al* 2019 High-definition visible-SWIR InGaAs image sensor using Cu-Cu bonding of III-V to silicon wafer *2019 IEEE Int. Electron Devices Meeting (IEDM)* pp 16.7.1–4

[5] Bhan R K and Dhar V 2019 Recent infrared detector technologies, applications, trends and development of HgCdTe based cooled infrared focal plane arrays and their characterization *Opto-Electron. Rev.* **27** 174–93

[6] Kalugin N G, Jing L, Bao W, Wickey L, Christopher D B, Ovezmyradov M, Shaner E A and Lau C N 2011 Graphene-based quantum Hall effect infrared photodetector operating at liquid Nitrogen temperatures *Appl. Phys. Lett.* **99** 013504

[7] Luque A and Marti A 1997 Increasing the efficiency of ideal solar cells by photon induced transitions at intermediate levels *Phys. Rev. Lett.* **78** 4

[8] Luque A, Martí A, Antolín E and Tablero C 2006 Intermediate bands versus levels in non-radiative recombination *Physica B* **382** 320–7

[9] Berencén Y, Prucnal S, Liu F, Skorupa I, Hübner R, Rebohle L, Zhou S, Schneider H, Helm M and Skorupa W 2017 Room-temperature short-wavelength infrared Si photodetector *Sci. Rep.* **7** 43688

[10] García-Hemme E *et al* 2022 On the optoelectronic mechanisms ruling Ti-hyperdoped Si photodiodes *Adv. Electron. Mater.* **8** 2100788

[11] Mailoa J P *et al* 2014 Room-temperature sub-band gap optoelectronic response of hyperdoped silicon *Nat. Commun.* **5** 3011

[12] Gandhi H H *et al* 2020 Gold-hyperdoped germanium with room-temperature sub-band-gap optoelectronic response *Phys. Rev. Appl.* **14** 064051

[13] Gandhi H H *et al* 2020 Chalcogen-hyperdoped germanium for short-wavelength infrared photodetection *AIP Adv.* **10** 075028

[14] Calvani P, Bellucci A, Girolami M, Orlando S, Valentini V, Polini R and Trucchi D M 2016 Black diamond for solar energy conversion *Carbon* **105** 401–7

[15] Dong X, Qiao R, Wang T, Yipeng A and Wang Y 2022 Engineering a bandgap-regulable intermediate-band material based on diamond *Carbon* **191** 106–11

[16] Ma S-X, Liu X-L, Sun H-B, Zhao Y, Yue H, Ning Xi-J, Zhao Li and Zhuang J 2020 Enhanced responsivity of co-hyperdoped silicon photodetectors fabricated by femtosecond laser irradiation in a mixed SF$_6$/NF$_3$ atmosphere *J. Opt. Soc. Am.* B **37** 730–5

[17] Tyler W W 1959 Deep level impurities in germanium *J. Phys. Chem. Solids* **8** 59–65

[18] Holland O W, Appleton B R and Narayan J 1983 Ion implantation damage and annealing in germanium *J. Appl. Phys.* **54** 2295–301

[19] Romano L, Impellizzeri G, Tomasello M V, Giannazzo F, Spinella C and Grimaldi M G 2010 Nanostructuring in Ge by self-ion implantation *J. Appl. Phys.* **107** 084314

[20] Impellizzeri G, Romano L, Bosco L, Spinella C and Grimaldi M G 2012 Nanoporosity induced by ion implantation in germanium thin films grown by molecular beam epitaxy *Appl. Phys. Express* **5** 035201

[21] Olea J, González-Díaz G, Pastor D, Mártil I, Martí A, Antolín E and Luque A 2011 Two-layer Hall effect model for intermediate band Ti-implanted silicon *J. Appl. Phys.* **109** 063718

[22] Kase M, Kikuchi Y, Kimura M, Mori H and Liebert R B 1994 Defects produced in Si $p^{+}n$ diodes by B^{+} implantation at liquid nitrogen temperature or $-60\,^{\circ}$C *J. Appl. Phys.* **75** 3358–64

[23] O'Leary S K, Zukotynski S and Perz J M 1997 Disorder and optical absorption in amorphous silicon and amorphous germanium *J. Non-Cryst. Solids* **210** 249–53

[24] Olea J, del Prado A, Pastor D, Mártil I and González-Díaz G 2011 Sub-bandgap absorption in Ti implanted Si over the Mott limit *J. Appl. Phys.* **109** 113541

[25] García-Hemme E, García-Hernansanz R, Olea J, Pastor D, Alvaro del P, Mártil I and Germán G-Díaz 2015 Meyer Neldel rule application to silicon supersaturated with transition metals *J. Phys. D: Appl. Phys.* **48** 075102